

# Fabrication and Analysis of Spatially Uniform Field Electrokinetic Flow Devices: Theory and Experiment

Andrew J. Skulan,\* Louise M. Barrett, Anup K. Singh, Eric B. Cummings, and Gregory J. Fiechtner

Sandia National Laboratories, Livermore, California 94551

A uniform-field design approach can improve the performance of microanalytical, chip-based devices for a number of applications, including separations and sample preparation. The faceted prism paradigm allows the design of microfluidic devices possessing spatially uniform fields in electrokinetically driven flows. We present the first quantitative study of the velocity fields obtained using faceted interfaces between deep and shallow channel sections. Electrokinetic flows were generated in a series of wet-etch fabricated microfluidic channels. The resulting velocity fields were analyzed by particle image velocimetry and compared with simulations of the two-dimensional Laplace equation using both the designed channel geometry and the as-fabricated channel geometry. This analysis found localized differences between the designed and observed flow fields that were directly attributable to the limitations of isotropic substrate etching. Simulations using the as-fabricated channel geometry reproduced the experimental electrokinetic velocity field, quantitatively accounting for speed field variations due to the limits of the fabrication method. The electrokinetic speed fields were also compared to corresponding pressure-driven speed fields.

Microfluidic devices promise to allow a broad range of chemical and medicinal analyses using small sample volumes in compact, low-cost, and easily manufactured devices.<sup>1,2</sup> The development of multifunctional, highly integrated micro total analysis systems ( $\mu$ TAS)<sup>3–5</sup> will require methodologies that allow rational channel design for the control of fluid flow.

A novel method of channel design is based on faceted prisms (Figure 1).<sup>6,7</sup> Faceted channels consist of a concatenation of ridges of distinct depths. An example ridge is illustrated in the three-dimensional drawing of Figure 1a, in which a fluid enters via a

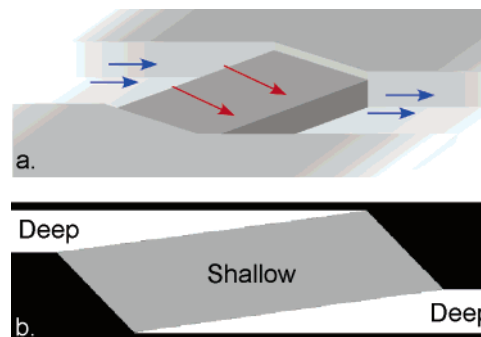


**Figure 1.** (a) Three-dimensional illustration of a flow displacer faceted channel; (b) faceted channel depth profile (top view). The blue arrows in the deep regions of (a) indicate a slower flow velocity relative to the shallow region above the ridge (red arrows).

deep channel section, passes through a shallow region formed by an insulating ridge, and exits through a deep channel. A corresponding top view of the ridge is shown in Figure 1b. Such geometries allow the generation of spatially uniform flow fields in each channel section (inlet, outlet, each ridge segment) under ideal electrokinetic flow conditions. They utilize the variation in specific permeability that arises from the corresponding variation of channel depth and use simple trigonometric relations to allow precision design of spatially uniform electrokinetic flows in turns, flow displacers, flow splitters, and more exotic geometries.

A major design consideration in  $\mu$ TAS separation devices is dispersion minimization.<sup>8</sup> Under ideal conditions, a microfluidic separations element releases concentrated, fully resolved bands of each analyte. Experimentally, this efficiency is limited by diffusion, electric field inhomogeneity, and dispersion due to the channel geometry, decreasing the analytical resolution of these devices. Previous efforts to minimize this effect include the following: narrowing the channel at turns;<sup>9–13</sup> using complementary pairs of turns to cancel the dispersion in one turn;<sup>14</sup> using large-radius curves;<sup>14–16</sup> and differentially fabricating the side walls,

\* To whom correspondence should be addressed. E-mail: ajskula@sandia.gov.

- (1) Ehrfeld, W.; Hessel, V.; Lowe, H. *Microreactors: New Technology for Modern Chemistry*; Wiley-VCH: Weinheim, 2000.
- (2) Andersson, H.; van den Berg, A. *Sens. Actuators, B* **2003**, *92*, 315–325.
- (3) Kikutani, Y.; Hibara, A.; Uchiyama, K.; Hisamoto, H.; Tokeshi, M.; Kitamori, T. *Lab Chip* **2002**, *2*, 193–196.
- (4) Kikutani, Y.; Hisamoto, H.; Tokeshi, M.; Kitamori, T. *Lab Chip* **2004**, *4*, 328–332.
- (5) Paegel, B. M.; Emrich, C. A.; Weyemayer, G. J.; Scherer, J. R.; Mathies, R. A. *Proc. Natl. Acad. Sci. U.S.A.* **2002**, *99*, 574–579.
- (6) Fiechtner, G. J.; Cummings, E. B. *J. Chromatogr., A* **2004**, *1027*, 245–257.
- (7) Fiechtner, G. J.; Cummings, E. B. *Anal. Chem.* **2003**, *75*, 4747–4755.

- (8) Zubritsky, E. *Anal. Chem.* **2000**, *72*, 687A–690A.
- (9) Paegel, B. M.; Hutt, L. D.; Simpson, P. C.; Mathies, R. A. *Anal. Chem.* **2000**, *72*, 3030–3037.
- (10) Petersen, N. J.; Mogensen, K. B.; Kutter, J. P. *Electrophoresis* **2002**, *23*, 3528–3536.
- (11) Mogensen, K. B.; Petersen, N. J.; Hubner, J.; Kutter, J. P. *Electrophoresis* **2001**, *22*, 3930–3938.
- (12) Molho, J. I.; Herr, A. E.; Mosier, B. P.; Santiago, J. G.; Kenny, T. W.; Brennen, R. A.; Gordon, G. B.; Mohammadi, B. *Anal. Chem.* **2001**, *73*, 1350–1360.
- (13) Griffiths, S. K.; Nilson, R. H. *Anal. Chem.* **2001**, *73*, 272–278.

either with coatings or with geometrical obstructions to slow the flow on the inside of the curve and to compensate for the differences in path length.<sup>17,18</sup> The faceted channel approach is ideally suited to addressing this problem and has been explored theoretically.<sup>6,7</sup>

Other on-chip processes that can benefit from spatially uniform flow designs are filtration and concentration, especially when this is performed using insulating dielectrophoresis (IDEP). IDEP arises when a gradient in an electric field is created by introducing insulating obstructions.<sup>19–24</sup> While these methods have displayed batchwise concentration and separation, we have recently demonstrated continuous separation and concentration of a mixture of bacterial cells and latex nanospheres by a novel channel designed using the faceted prism design methodology.<sup>25</sup> This device operates in a voltage regime where the nonlinear dielectrophoretic contribution to particle motion is significant near the interface between the deep channel and the shallow faceted prism. Other potential applications of the faceted prism methodology include flow splitters that minimize dispersion for applications such as multidimensional separations or delivery to shallow channels for evanescent analyte detection with minimal dispersion.<sup>6</sup>

To create microfluidic devices, a number of micromanufacturing methods<sup>26</sup> (including wet-etching,<sup>3,27–30</sup> laser ablation,<sup>31,32</sup> embossing,<sup>33–36</sup> injection molding,<sup>37–39</sup> and micromachining<sup>40–42</sup>)

can be employed to construct channels containing ridges, each possessing practical limitations in precision. Because it is employed widely in the construction of  $\mu$ TAS devices,<sup>3,27,29,30,43</sup> and is readily available in our laboratory, the isotropic, wet-etching technique is used to construct channels in this study. Isotropic etching cannot generate sharp corners, rather forming rounded corners whose radii are proportional to the etch depth.<sup>44</sup>

In this paper, we present the first experimental demonstration of the fields that result when using the faceted prism technique. The deviation from spatially uniform flow behavior is examined for a series of faceted microchannels upon wet-etch device fabrication. The three channel geometries presented are a straight, faceted channel, in which the faceted interface is perpendicular to the side walls; a flow displacer channel such as that shown in Figure 1 that is useful in both flow control and concentration applications; and a flow divider that splits a fluid stream into two separate, parallel conduits. The deviation from ideal, spatially uniform behavior due to a wet-etch fabrication method is reflected in variations of the velocity field. To our knowledge, this is the first presentation of the experimental examination of microchannels designed using a simple, field-based methodology. To assess the magnitude of the deviation from a spatially uniform velocity field by experimental means, particle image velocimetry (PIV)<sup>45–47</sup> is used to obtain velocity fields. These experimental velocity fields are compared to simulations of the Laplace equation based on the experimental geometries. The simulations serve as a tool to aid the analysis of the experimental velocity fields and verify that the deviations from spatially uniform fields are caused by limitations in fabrication rather than deviations from ideal electrokinetic flow.

Another factor that commonly interferes with pure electrokinetic velocity fields is pressure-driven flow.<sup>48,49</sup> This is a difficult effect to eliminate and becomes important during device operation as a result of reservoir-depth imbalance at microchannel inlet and outlet ports. Since our design methodology assumes the presence of ideal electrokinetic flow,<sup>6,7,22,50</sup> we also examine the differences between pressure-driven and electrokinetic flows at a ridge.

## EXPERIMENTAL SECTION

**Fabrication.** The glass channels used in this study were designed and fabricated in-house using standard photolithography, wet-etch, and bonding techniques. The microchips were fabricated from Schott D263 glass wafers (100-mm diameter, 1.1-mm thick,

- (14) Culbertson, C. T.; Jacobson, S. C.; Ramsey, J. M. *Anal. Chem.* **1998**, *70*, 3781–3789.
- (15) Griffiths, S. K.; Nilson, R. H. *Anal. Chem.* **2002**, *74*, 2960–2967.
- (16) Culbertson, C. T.; Jacobson, S. C.; Ramsey, J. M. *Anal. Chem.* **2000**, *72*, 5814–5819.
- (17) Johnson, T. J.; Ross, D.; Gaitan, M.; Locascio, L. E. *Anal. Chem.* **2001**, *73*, 3656–3661.
- (18) Dutta, D.; Leighton, D. T. *Anal. Chem.* **2002**, *74*, 1007–1016.
- (19) Benguigui, L.; Lin, I. J. *J. Appl. Phys.* **1984**, *56*, 3294–3297.
- (20) Chou, C. F.; Zenhausern, F. *IEEE Eng. Med. Biol. Mag.* **2003**, *22*, 62–67.
- (21) Suehiro, J.; Zhou, G. B.; Imamura, M.; Hara, M. *IEEE Trans. Ind. Appl.* **2003**, *39*, 1514–1521.
- (22) Cummings, E.; Singh, A. *Anal. Chem.* **2003**, *75*, 4724–4731.
- (23) Lapizco-Encinas, B. H.; Simmons, B. A.; Cummings, E. B.; Fintschenko, Y. *Anal. Chem.* **2004**, *76*, 1571–1579.
- (24) Lapizco-Encinas, B. H.; Simmons, B. A.; Cummings, E. B.; Fintschenko, Y. *Electrophoresis* **2004**, *25*, 1695–1704.
- (25) Barrett, L. M.; Skulan, A. J.; Singh, A. K.; Cummings, E. B.; Fiechtner, G. *J. Anal. Chem.* **2005**, *77*, 6798–6804. ac0507791
- (26) Bruin, G. J. M. *Electrophoresis* **2000**, *21*, 3931–3951.
- (27) West, J. A. A.; Lane, T. W.; Stamps, J. F.; Shokair, I. R.; Freutel, J. A. 7th International Conference on Micro Total Analysis Systems, Squaw Valley, CA, MESA Monographs; 2003; pp 143–146.
- (28) Jacobson, S. C.; Hergenroder, R.; Moore, A. W.; Ramsey, J. M. *Anal. Chem.* **1994**, *66*, 4127–4132.
- (29) Liu, R. H.; Stremmer, M. A.; Sharp, K. V.; Olsen, M. G.; Santiago, J. G.; Adrian, R. J.; Aref, H.; Beebe, D. J. *J. Microelectromech. Syst.* **2000**, *9*, 190–197.
- (30) Roulet, J. C.; Volkell, R.; Herzig, H. P.; Verpoorte, E.; de Rooij, N. F.; Dandliker, R. *Anal. Chem.* **2002**, *74*, 3400–3407.
- (31) Roberts, M. A.; Rossier, J. S.; Bercier, P.; Girault, H. *Anal. Chem.* **1997**, *69*, 2035–2042.
- (32) Rossier, J.; Reymond, F.; Michel, P. E. *Electrophoresis* **2002**, *23*, 858–867.
- (33) Johnson, T. J.; Waddell, E. A.; Kramer, G. W.; Locascio, L. E. *Appl. Surf. Sci.* **2001**, *181*, 149–159.
- (34) Gerlach, A.; Knebel, G.; Guber, A. E.; Hecke, M.; Herrmann, D.; Muslija, A.; Schaller, T. *Sens. Mater.* **2002**, *14*, 119–128.
- (35) Chen, Z. F.; Gao, Y. H.; Lin, J. M.; Su, R. G.; Xie, Y. *J. Chromatogr., A* **2004**, *1038*, 239–245.
- (36) Becker, H.; Heim, U. *Sens. Mater.* **1999**, *11*, 297–304.
- (37) McCormick, R. M.; Nelson, R. J.; Alonso-Amigo, M. G.; Benvegna, J.; Hooper, H. H. *Anal. Chem.* **1997**, *69*, 2626–2630.
- (38) Edwards, T. L.; Mohanty, S. K.; Edwards, R. K.; Thomas, C. L.; Frazier, A. B. *Sens. Mater.* **2002**, *14*, 167–178.
- (39) Hulme, J. P.; Mohr, S.; Goddard, N. J.; Fielden, P. R. *Lab Chip* **2002**, *2*, 203–206.

- (40) Fan, Z. H.; Harrison, D. J. *Anal. Chem.* **1994**, *66*, 177–184.
- (41) Fister, J. C.; Jacobson, S. C.; Davis, L. M.; Ramsey, J. M. *Anal. Chem.* **1998**, *70*, 431–437.
- (42) Harrison, D. J.; Fluri, K.; Seiler, K.; Fan, Z. H.; Effenhauser, C. S.; Manz, A. *Science* **1993**, *261*, 895–897.
- (43) Sun, K.; Yamaguchi, A.; Ishida, Y.; Matsuo, S.; Misawa, H. *Sens. Actuators, B* **2002**, *84*, 283–289.
- (44) Madou, M. *Fundamentals of Microfabrication*; CRC Press LLC: Boca Raton, FL, 1997.
- (45) Santiago, J. G.; Wereley, S. T.; Meinhart, C. D.; Beebe, D. J.; Adrian, R. J. *Exp. Fluids* **1998**, *25*, 316–319.
- (46) Devasenathipathy, S.; Santiago, J. G.; Wereley, S. T.; Meinhart, C. D.; Takehara, K. *Exp. Fluids* **2003**, *34*, 504–514.
- (47) Cummings, E. B. *Experiments in Fluids*; 3rd International Workshop on Particle Image Velocimetry; September 16–18, 1999; Santa Barbara, CA. **2000**, *29*, S42–S50.
- (48) Santiago, J. G. *Anal. Chem.* **2001**, *73*, 2353–2365.
- (49) Herr, A. E.; Molho, J. I.; Santiago, J. G.; Mungal, M. G.; Kenny, T. W.; Garguilo, M. G. *Anal. Chem.* **2000**, *72*, 1053–1057.
- (50) Patankar, N. A.; Hu, H. H. *Anal. Chem.* **1998**, *70*, 1870–1881.

S. I. Howard Glass Co., Worcester, MA). The photomasks were designed using DW-2000 (Design Workshop Technologies., Montreal, Canada) and fabricated by Photo Sciences Inc., (Torrance, CA). D263 borosilicate wafers were sputter-deposited (Cooke Vacuum Products., South Norwalk, CT) with chromium metal to a thickness of 200 nm, which served as the hard mask. The mask defined a total of 16 channels of varying geometry, and each geometry was represented at least three times on the chip, for a total of 50 channels/chip. Three of these channel designs are described in this study. A 7.5- $\mu\text{m}$ -thick layer of SJR 5740 (Shipley Corp., Marlborough, MA) positive photoresist was spin-coated on the wafer and soft-baked at 90 °C for 5 min. The mask pattern was transferred to the photoresist by exposure to UV light in a contact mask aligner at 775  $\mu\text{J}/\text{mm}^2$ . Exposure time varied depending on flux intensity (MA-6, Karl Suss America Inc., Waterbury Center, VA). After exposure, the photoresist was developed with Microposit developer concentrate (Shipley Corp.) and hard-baked for 30 min at 125 °C. Exposed chromium was etched with CEN 300 Microchrome etchant (Microchrome Technologies Inc., San Jose, CA). The resulting exposed glass was etched with a 16% HF solution (Shape Products Co., Oakland, CA), and the remaining chrome was removed. This process was repeated to generate a two-level etched device. The mask for the second etch was aligned with the first etch through the use of a pair of alignment marks located near the outer edges of the wafer. The alignment marks on the mask were overlaid with those on the wafer using a MA-6 Karl Suss aligner. The exposure time to the etchant was controlled to achieve a particular etch depth. The exposure time of the first etch was 9 times that of the second etch, resulting in a device with deep channels 10 times as deep as the facet depth. Via access holes were drilled in the cover plate (D263 Glass) with diamond-tipped drill bits (Amplex, Worcester, MA). The etched wafer and drilled cover plate were cleaned with 4:1  $\text{H}_2\text{SO}_4/\text{H}_2\text{O}_2$  (100 °C). The machined cover plate were rinsed with 1% HF solution to inhibit crack propagation. The substrates were then immersed into an 80 °C 40% NaOH solution, rinsed in a cascade bath, spun dry, aligned for contact, and thermally bonded by slowly ramping the temperature to 610 °C for 5 h in a nitrogen-purged programmable muffle furnace (model 48000, Thermolyne, Dubuque, IA).

The channels consist of a facet located in the center of a 10.2-mm-long channel (Figure 2a). The inlet and outlet channels are accessed by 500- $\mu\text{L}$  entrance and exit reservoirs. The designed facet depth is 5  $\mu\text{m}$  ( $d_2$  in Figure 2c), and the channel depth is 50  $\mu\text{m}$  ( $d_1$  in Figure 2c). The channel geometries display constant-radius curvature at the walls (Figure 2b) where the radius equals the 50- $\mu\text{m}$  etch depth ( $d_1$  in Figure 2c), which results from the use of an isotropic wet-etch during channel fabrication.

**Data Acquisition and Reduction.** The channels were filled with 200-nm-diameter, green, fluorescently labeled latex beads (carboxylate modified FluoSpheres from Molecular Probes, Inc) diluted to 0.2% in deionized water (adjusted to pH 7.83 with NaOH). Electrokinetic flows were generated by applying a voltage across a channel whose reservoirs had been volume-equilibrated to eliminate concurrent pressure-driven flow. Voltage was applied through two platinum electrodes attached to an E3630A power supply (Agilent Technologies, Inc, Palo Alto, CA). The applied potentials for the data presented are straight (3 V/cm), displacer

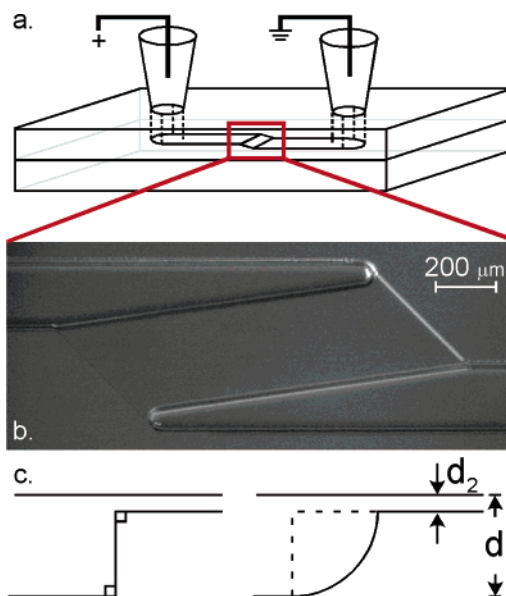


**Figure 2.** (a) Microchannel geometry, including fluid reservoirs, (b) top-illuminated image of the “displacer” channel, and (c) side-view illustration of an as-designed (left) and isotropic wet-etch ridge profile (right). The ratio of deep channel to ridge depth,  $d_1:d_2$  is 10:1.

(6 V/cm), and splitter (3 V/cm). Pressure-driven flows were generated by making the reservoir volumes on the inlet and outlet channels unequal (head difference  $\sim 1$  mm). Images of bead behavior were recorded using an IX70 inverted epifluorescence microscope with attached Cohu 4910 CCD camera (Cohu, Inc., San Diego, CA). CCD pixel size is 9- $\mu\text{m}$  square. Microscope magnifications for images presented are straight ( $\times 20$ ), displacer ( $\times 10$ ), and splitter ( $\times 20$ ) channel, leading to spatial resolutions of 0.45, 0.90, and 0.45  $\mu\text{m}$ , respectively. Following the approach of Meinhart et al.,<sup>51</sup> we calculate a depth of correlation of 11.2 ( $\times 20$ ) and 19.3  $\mu\text{m}$  ( $\times 10$ ) for our experimental setup. The focal plane is located at the center of the shallow facet in each experiment. Thus, for each channel geometry presented, the full cross section of the shallow faceted region contributes to the PIV analysis. In the deep section, particles contribute to the PIV analysis if they are within 12.2 ( $\times 10$  objective) or 8.1  $\mu\text{m}$  ( $\times 20$  objective) of the top of the channel. The successive image frames were recorded at 30 frames/s at 640  $\times$  480 pixels/image.

Successive image frames were analyzed using two pieces of software: the FlowManager Particle Image Velocimetry software package (Dantec Dynamics, Inc) and a PIV code developed in-house.<sup>47</sup> For the FlowManager analysis, interpolations between successive frames were made using a cross-correlation method employing 16  $\times$  16 pixel interrogation areas and requiring 75% overlap. Flow data for the first 5 s following the application of voltage were discarded as they may be distorted by initial flow equilibration or electric field stabilization. The images from the next  $\sim 20$  s were averaged to generate the velocity fields presented below, resulting in greater than 250 correlated pairs of flow images contributing to each velocity field. The pressure-driven flow resulting from the pressure head generated by 25 s of electrokinetic flow was less than 3% of the electrokinetic velocity. To verify that the lower resolution PIV method delivered an accurate

(51) Meinhart, C. D.; Wereley, S. T.; Gray, M. H. B. *Meas. Sci. Technol.* **2000**, *11*, 809–814.

representation of the velocity field (e.g., near regions of sharp electric field gradients), the Sandia code was used and achieved single-pixel resolution through a correlation-averaging approach. This process was repeated for multiple copies of the channels presented in this study on two separate chips.

**Simulations.** The electrokinetic flow was simulated using the Sandia “Laplace” electrokinetic and dielectrophoretic simulation code.<sup>6,7,22,52</sup> The Laplace simulation package simulates ideal electrokinetic flows by solving the modified Laplace equation  $\sigma(x,y)\nabla\varphi(x,y) = 0$  for the velocity/electrostatic potential  $\varphi$  on a quasiplanar domain defined by the field  $\sigma$ . This is applicable as the channel dimensions, applied potentials, and other experimental variables approach the ideal electrokinetic limit.<sup>53,54</sup> This allows the electrokinetic potentials (and their associated speed fields) to be described for a given channel geometry. The ideal geometries included three channel depths: wall ( $0\ \mu\text{m}$  deep), inlet and outlet channels ( $50\ \mu\text{m}$  deep), and facet ( $5\ \mu\text{m}$  deep). The boundaries between these regions are sharp, reflecting the geometry shown in Figure 1c, left. Simulations of the as-fabricated geometries possessed the same three depths, but gradients were included at the boundaries between different depth regions, as required by isotropic etching (Figure 2c, right). For convenience, this arc was approximated by a half-Gaussian curve.

## RESULTS AND ANALYSIS

**Straight Channel.** The simplest uniform-field channel design has faceted interfaces oriented perpendicular to the inlet and outlet channel walls.<sup>6,7</sup> By employing this trivial design, the influence of complicating factors such as angled flows and rounded-turn corners can be eliminated from the study of velocity-field uniformity, allowing the impact of manufacturing offset and variability to be studied. The velocity field predicted by the Laplace simulation for such a trivial, ideal channel has two regions: a uniform, slow velocity in deep channel sections (depicted as blue in Figure 3a) and a uniform, fast velocity in the shallow faceted prism (depicted as red in Figure 3a). This ideal design has a shallow section of  $5\text{-}\mu\text{m}$  depth and deep inlet and outlet sections of  $50\text{-}\mu\text{m}$  depth. Since the speeds in the shallow and deep sections are related by continuity,<sup>6,7</sup> the speed in the shallow section is 10 times that of the deep sections. The corresponding experimentally measured velocity field is shown in Figure 3b (the microscope objective was centered over the right-hand side of the facet of Figure 3a). Here, the velocity fields in both deep and shallow sections are found to be substantially uniform, with the fluid moving quickly in the shallow faceted prism (red) and slowly in the deep channel section (blue). The ratio of average velocity (averaging the velocity along a line across the channel, normal to the side walls) in the shallow facet to that in the deep section is 16:1. Part of this discrepancy results from a mask offset in which the deep section is 20% too wide (when compared to the ideal channel of Figure 3a). Correcting for this offset using continuity, the resulting effective velocity ratio becomes 13:1, which remains larger than the ideal ratio. This deviation from design dimensions arises from errors in the etch time and sagging of the channel

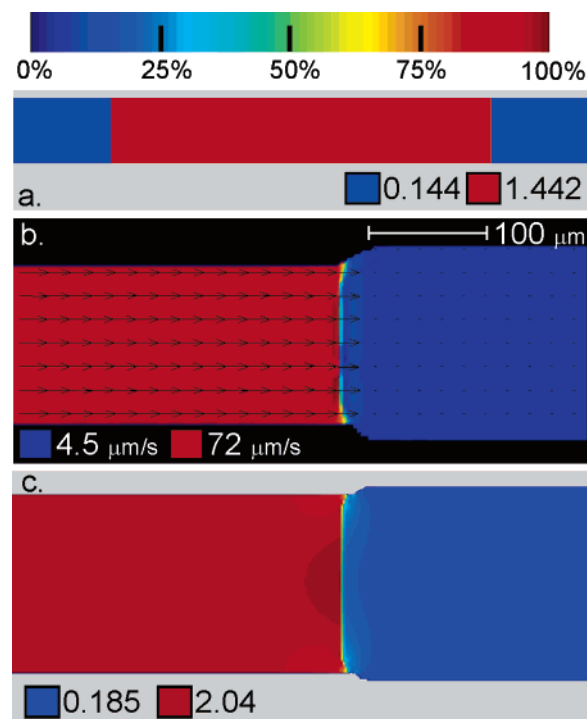


**Figure 3.** (a) Laplace simulation of the as-designed straight-channel velocity field. The ratio of deep channel to ridge fluid depths in the simulation is 10:1. (b) Experimental PIV velocity field of the 50:5- $\mu\text{m}$  straight channel. (c) Laplace simulation of the as-fabricated straight-channel velocity field. The simulation velocity is in arbitrary units. The look-up table at the top of the figure is the same one used throughout this paper. Royal blue has a speed of 0 (in the appropriate units for the figure) while burgundy is 100% of the speed scale chosen for a particular figure.

roof during the thermal bonding process. The spatial near-uniformity of the experimental PIV result in both the deep channel and the shallow region indicates that the deviation from ideal behavior in the straight channel geometry is minimal and is limited to the relative magnitudes of the fluid flow in the shallow and deep channel sections.

The simulation of the as-fabricated straight channel geometry (Figure 3c) is qualitatively the same as the experimental velocity field (Figure 3b) and also shows that the etch effect on the velocity field is small, as seen by comparison to the designed channel simulation (Figure 3a). The small gradient at the facet corners in the experimental velocity field is anticipated by the as-fabricated simulation due to the change in cross-sectional area that occurs upon entering and leaving the facet. In the as-designed case, the velocity change is spatially abrupt at the interface due to the constant channel width and the channel walls and floor being perpendicular (Figure 2c, left), while the as-fabricated simulation shows a spatial gradient in the velocity field. This gradient extends  $45\ \mu\text{m}$  (the length of the isotropic-etch wall-arc—corresponding to  $(d_1 - d_2)$  in Figure 2c, right) away from the facet.

**Displacer Channel.** A displacer element translates a channel perpendicular to the direction of fluid flow, with the input and output flows traveling parallel to one another (Figure 1 a, b). It forms the base element for faceted prism turns and expanders.<sup>6,7</sup> It also represents the primary element for insulating-ridge devices based on faceted prisms that perform particle filtration and concentration using dielectrophoresis.<sup>25</sup> The velocity field of a

(52) Cummings, E. B.; Griffiths, S. K.; Nilson, R. H.; Sandia National Laboratories: Livermore, CA, Vol. SAND 2002–8018; 2001; pp 65–93.

(53) Cummings, E. B.; Griffiths, S. K.; Nilson, R. H.; Paul, P. H. *Anal. Chem.* **2000**, *72*, 2526–2532.

(54) MacInnes, J. M. *Chem. Eng. Sci.* **2002**, *57*, 4539–4558.

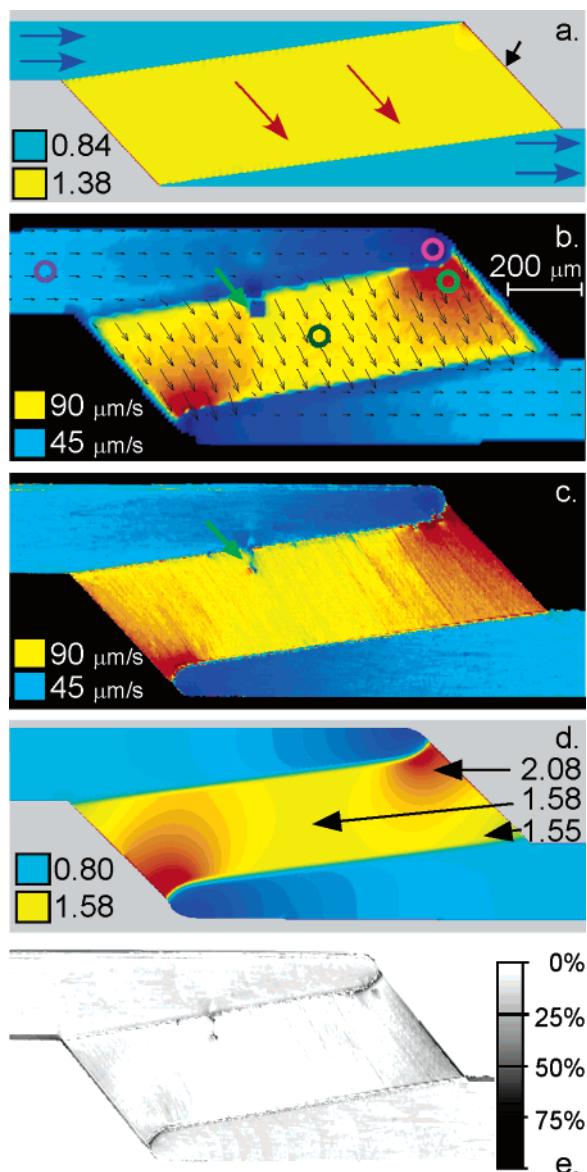


**Figure 4.** (a) Laplace simulation of the as-designed displacer channel velocity field. The ratio of deep channel to ridge fluid depths in the simulation is 10:1. The blue and red arrows indicate the flow directions; the small black arrow highlights the red pixels that are an artifact of the numerical simulation grid. (b) Experimental PIV velocity field using  $16 \times 16$  pixel resolution of the  $50:5\text{-}\mu\text{m}$  displacer channel. The green arrow highlights a particle aggregate that has become lodged in the facet. The velocity in the magenta circle is 8% of that in the purple circle; the velocity in the light green circle is 33% greater than that in the dark green circle. (c) Experimental PIV velocity field of the  $50:5\text{-}\mu\text{m}$  displacer channel using single-pixel resolution. The same data set was used for (b) and (c). (d) Laplace simulation of the as-fabricated displacer channel velocity field. The simulation velocities are in arbitrary units. (e) Difference map of the experimental (c) and simulated (d) velocity fields.

displacer element, designed using the spatially uniform, faceted prism approach, is shown in Figure 4a. The slight speed-field variation indicated by the color variation along the facet–sidewall connection (red, highlighted by black arrow) is caused by the finite numerical resolution of the simulation, as is the minor, sawtooth color variation (darker blue) at the facet–channel interface.

The corresponding experimental electrokinetic velocity field in the displacer channel (Figure 4b) is largely uniform. The two regions that deviate from this behavior are found in the rounded corners generated by wet-etch channel fabrication (top-right and bottom-left of the channel) and the adjacent region in the facet. The same behavior is observed in the symmetry-related exit to the facet (bottom-left of the facet in Figure 4b). The slow speed in the acute corner of the deep channel (magenta circle in Figure 4b) is 8% of that in the middle of the inlet (purple circle in Figure 4b), while the adjacent fast speed at the edge of the facet is 33% greater than that in the center of the facet (light green and dark green circles in Figure 4b, respectively).

To explore further the observed field variations and the slow velocity in one interrogation box (which appears as a square blue box in the low-resolution data analysis of Figure 4b and is due to a lodged bead agglomeration), the PIV analysis was repeated using the single-pixel analysis code. As shown in Figure 4c, high-resolution analysis identifies the same variations in the velocity field across the faceted prism and indicates that the use of a larger interrogation box reliably represents the channel's velocity field. Single-pixel analysis shows that the flow nonuniformity about the lodged agglomeration of particles is limited spatially to the particle location, as indicated by the green arrow of Figure 4c, where the spatial extent of the disturbance is  $\sim 230 \mu\text{m}^2$ . Additionally, use of the single-pixel code allows fields to be interrogated immediately adjacent to the faceted interfaces where manufacturing anomalies (such as cracks or roughness in the facet face) can occur. The anomalous alternating yellow and orange streaks that appear in the field for the shallow, faceted prism of Figure 4c are an artifact of the analysis code, which weights the integrated fluorescence intensity of large-particle agglomerates more than that for individual beads. Because the lower resolution software is sufficient to interrogate the fields for the present study, and because of the prohibitive run time required to use the high resolution code, we avoid using data for which polystyrene particles lodge in channels at substantial levels. Such channel fouling becomes more prevalent as a given microchannel undergoes repeated use, requiring the use of a fresh channel for the present studies. Having obtained the field variation experimentally, the 2D Laplace solver was used to simulate the velocity field of the as-fabricated displacer channel, resulting in the velocity field shown in Figure 4d. The field distribution obtained using the simulation is similar to the experimental fields of Figure 4b and c. The fluid speed in the facet varies by 32% between the middle of the facet and the faster region in the corner (Figure 4d), while the experimental speed difference between these two points (green circles in Figure 4b) is 33%. This agreement is reinforced by the image of Figure 4e, which represents a difference map between panels c and d, after normalizing the relative field magnitudes. As shown, the local difference between the experimental and numerical relative speed-field maps is less than 5%. This observation shows that deviations from ideal design caused by manufacturing limitations can be accounted for in future designs by application of 2D simulations of physically relevant channel geometries.

**Splitter Channel.** Flow splitters are useful for performing multiple, parallel analyses on a single chip. Faceted prism designs

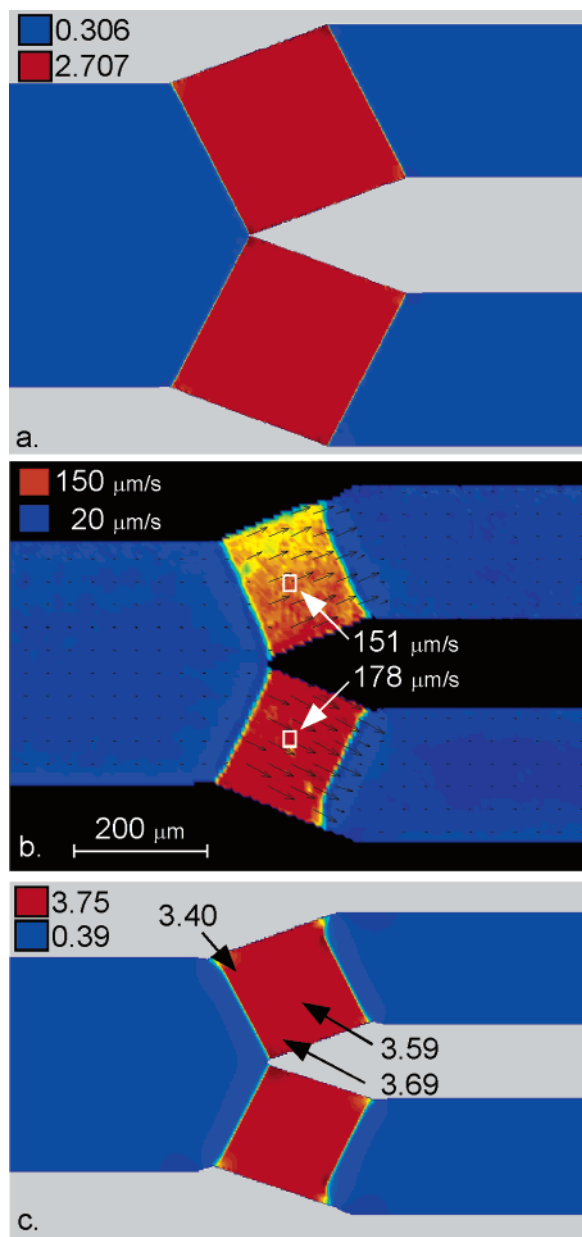


**Figure 5.** (a) Laplace simulation of the as-designed splitter channel velocity field. The ratio of deep channel to ridge fluid depths in the simulation is 10:1. (b) Experimental PIV velocity field using  $16 \times 16$  pixel resolution of the 50:5- $\mu\text{m}$  splitter channel. (c) Laplace simulation of the as-fabricated displacer channel velocity field. The simulation velocities are in arbitrary units.

can also be useful for constructing flow splitters capable of dividing an inlet flow into any number of outlet flows, while retaining spatially uniform field distributions.<sup>6</sup> Alternatively, faceted flow splitters can be operated in reverse to function as flow combiners.<sup>6</sup> When splitters and combiners are placed in sequence, they can be used to form benign channel supports within a wide microchannel.<sup>6</sup> Therefore, we have also examined the operation of a simple, two-way splitter (Figure 5). The electrokinetic speed field of an ideal flow splitter is shown in Figure 5a, displaying a uniform velocity in the deep channels (blue) and a faster, uniform velocity in the shallow, faceted prisms (red). The experimental velocity field is shown in Figure 5b. Here, the speed field in the top facet of the splitter is observed to be less than that in the lower facet

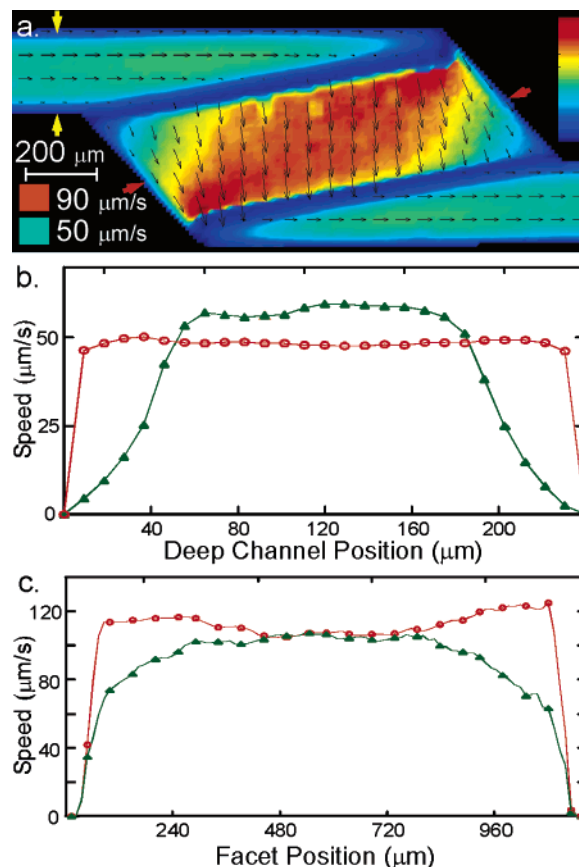


**Figure 6.** (a) PIV-derived hydrodynamic flow field of the displacer channel. (b), (c) Cross sectional speed profiles for electrokinetic (red) and pressure-driven (green) flow in the displacer channel geometry at two locations. The line joining the yellow arrows in (a) indicates where deep channel speed profiles shown in (b) were obtained. The line joining the orange arrows in (a) indicates where the shallow channel speed profiles shown in (c) were measured.

by  $\sim 15\%$ . This difference is consistent with a different depth in the two channels resulting from variability in etching within channels as a function of position across the substrate.

The simulated as-fabricated splitter channel velocity field with the same ridge depths in each shallow, faceted prism predicts a symmetric flow field, (Figure 5c) consistent with the above explanation. The deviation from spatial uniformity predicted for the splitter channel—the fluid velocity varies by 10% across the facet (Figure 5c)—is much less pronounced than for the displacer channel (30% variation as indicated in Figure 4d). This observation indicates that the variation in fluid speed depends not only upon the fabrication method but also upon the specific channel geometry.

**Pressure-Driven Flow.** The speed field of a pressure-driven flow through the displacer channel is shown in Figure 6a. For these pressure-driven flow experiments, the Reynolds number is below 0.01, such that flow is always laminar. The resulting flow field displays significant differences in comparison to the corresponding electrokinetic flow field (Figure 4b). During pressure-driven flow, the velocity across the channel (perpendicular to the flow direction) varies, with the speed at the center of the channel greater than that near the walls. This is caused by the influence

of drag at the walls of the channel<sup>55</sup> and the large surface-to-volume ratio of the present designs. This behavior is also observed in the shallow, faceted prism, with the middle of the channel exhibiting a greater speed than at the side walls.

The cross-sectional speed profiles of the electrokinetic versus pressure-driven flows were investigated in both the deep channel (line joining yellow arrows in Figure 6a, speed profile shown in Figure 6b) and the facet (line joining orange arrows in Figure 6a, speed profile shown in Figure 6c). The deep channel electrokinetic flow is comparatively uniform, rapidly decreasing to zero within 5  $\mu\text{m}$  of the side walls, well within the 50- $\mu\text{m}$  etch radius. In contrast, the deep channel pressure-driven speed field increases more slowly with increasing distance from the side walls, before leveling off 75  $\mu\text{m}$  from the walls. The cross-sectional electrokinetic speed field for the shallow, faceted prism is relatively less uniform than in the channel, displaying a slight dip in speed in the middle of the channel that is 18% lower than the maximum speed. Nevertheless, the electrokinetic flow profile remains quite flat, particularly when compared to the superimposed pressure-driven profile. This pressure-driven local variation in speed along a faceted interface could cause leakage of particles for a filter/concentrator where the design requires spatially uniform forces and is to be minimized accordingly.<sup>25</sup>

## DISCUSSION

The presence of the rounded corners caused by an isotropic etch fabrication method has been observed to lead to spatial variation in the velocity fields of three channel designs: straight, displacer, and splitter. The variation increased with incidence angle of the faceted interface; it was smallest for the straight channel where the facet face is normal to flow and greatest for the displacer channel, which had the largest incident angle of the three. Therefore, the fabrication method will place an upper bound on the incidence angle that can be employed for a device with a given tolerance for velocity variation.

Simulations were repeated to explore the magnitude of the etch effect on the cross-channel velocity profile. As the displacer channel velocity field was the most sensitive to isotropic etching of the three geometries presented, this channel was chosen as a test geometry. Figure 7a shows the change in channel geometry with an increase in the etch depth. The gray-scaled background is the as-designed geometry; the red, dashed line has an etch depth that is 9% of the displacer inlet channel width, while this value is 21% for the green, dashed line. The resulting cross-facet velocity profiles (corresponding to the line joining the orange arrows in Figure 6a) show faster speed near the walls and a slower speed in the middle (Figure 7b). This is consistent with the results of the  $\mu\text{PIV}$  experiments (Figure 6c). The shape of the velocity profile curves is quite similar for all curves except for the 21% etch/deep channel ratio whose maximum is closer to the center of the channel than the other etch depths. This results from an etch depth that approaches the magnitude of the channel width. The percentage variation in the velocity field across the channel increases linearly with etch depth for small etch depths, and the gradient decreases for larger etch depths (Figure 7c) as the deviation from the ideal geometry becomes greater. The linear

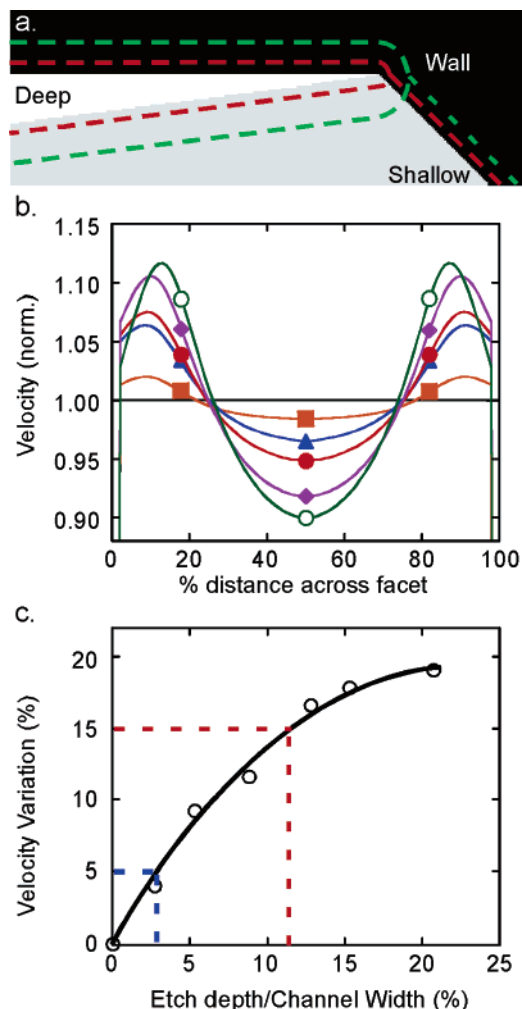


**Figure 7.** (a) Change in channel shape in the corner of the displacer channel with increasing etch depth. For the green dashed line the etch depth is 21% of the inlet channel width and the red dashed line etch depth is 9%. This is superimposed on the as-designed displacer channel geometry. (b) Fluid velocity across the middle of the facet in the displacer channel (the same line as denoted by the orange arrows in Figure 6a). Each line is the etch depth as a percentage of the deep-inlet channel width: 3 (orange/square), 5 (blue/triangle), 9 (red/circle), 13 (purple/diamond), and 21% (green/open circle). All velocities have been normalized to the same net flow through the facet. The three trace markers (open circle, etc.) for each line are included to aid comprehension. (c) Etch depth as a percentage of the inlet channel width vs percentage cross-facet velocity variation. The data points are the percentage difference between the maximum and minimum of the simulated velocity profiles shown in (b) (this excludes the zero velocity at the walls). The black line is a generic smooth fitting curve included for clarity. The dashed red line illustrates the maximum etch depth/channel depth ratio for a channel with 15% cross-facet velocity variation, while the dashed blue line corresponds to a 5% variation.

increase in simulated cross-facet velocity variation for small etch depths indicates that there is no threshold depth above which cross-facet velocity variations suddenly become prevalent and that should not be crossed when designing a spatially uniform electrokinetic flow channel.

Using such calculations, it is possible to estimate the tolerable etch depth with respect to the channel width based on relative deviation from velocity-field uniformity for a given location within a channel. For a device in which a 15% deviation of cross-facet velocity is acceptable ( $\sim\pm 7.5\%$  from the mean), the maximum etch

(55) Probstein, R. *Physicochemical Hydrodynamics*; John Wiley & Sons: New York, 1994.

depth is 12% of the channel width (illustrated by the red dashed lines in Figure 7c). Thus, if a channel width of 100  $\mu\text{m}$  is required, the etch depth must be 12  $\mu\text{m}$  or less. Conversely, to redesign the displacer channel to have a cross-facet velocity variation of less than 5% (blue dashed lines in Figure 7c), with a facet depth of 5  $\mu\text{m}$  and a 50- $\mu\text{m}$ -deep channel depth, the maximum etch depth is 3% of the channel width, requiring 1725- $\mu\text{m}$ -wide inlet and outlet channels.

The general channel design paradigm for minimizing spatial variation in the velocity field of channels constructed using the faceted prism approach is to minimize the ratio of the etch depth to channel width. This can be achieved by a combination of decreasing the etch depth, resulting in a smaller channel cross-sectional area, and increasing the channel width. The preferred magnitudes of these two parameters vary with the intended application and depend on the required fluid throughput, the size of species present in the fluid, and fabrication limitations.

The implications for separations applications are clear: dispersion leads to analyte band broadening, lowering the resolution and detection limit of the device. Skew-induced dispersion can be minimized using uniform-field design. For particle filtration applications using IDEP, the uniformity of velocity fields allows more precise balancing of electrokinetic and dielectrophoretic forces on particles across the entire length of an insulating ridge. This permits more sensitive tuning of device performance to allow the device to be used to separate mixtures of analytes.

## CONCLUSIONS

The present study represents the first quantitative experimental study of field uniformity for the faceted prism technique. The rational design and fabrication of controlled, ideal electrokinetic devices has been demonstrated for several geometries. The resulting experimental electrokinetic velocity fields have been quantitatively compared with the predictions of simple theoretical models. From this study, we conclude the following:

1. Deviations from exact mathematical designs result in velocity-field nonuniformity. In the case of isotropic etching, designs cannot be reproduced directly.

2. The resulting channels can be modeled reliably using simple, two-dimensional simulations. These simulations can be extended to estimate minimum channel depths or widths necessary to minimize field variation across-faceted prisms.

3. Pressure-driven flow, which cannot be simulated using the techniques shown in this paper, results in flow-field nonuniformity that is comparatively large and is to be minimized.

Two-dimensional simulation of channel geometries using ideal electrokinetic theory is a powerful tool for the rational design and optimization of electrokinetically driven microfluidic devices. When this approach is combined with experimental testing of theoretical predictions and integrated into the development phase, the resulting devices' performance promises to be greatly enhanced. A device based on such design is presented in a second paper, in which we demonstrate the filtration/concentration of particles.<sup>25</sup>

## ACKNOWLEDGMENT

The authors thank Boyd Wiedenman and John Brazzle (Sandia National Laboratories) for mask layout and design assistance. The authors also thank Susan Jamison, William Kleist, and George Sartor (Sandia National Laboratories) for chip construction. This work was supported by Sandia National Laboratories' Laboratory Directed Research and Development funding under the program management of Duane Lindner. Sandia is a multiprogram laboratory operated by Sandia Corp., a Lockheed-Martin company, for the United States Department of Energy under contract DE-AC04094AL85000.

Received for review May 5, 2005. Accepted August 19, 2005.

AC050777G